Statistics of Local and Global Flame Speed and Structure for Highly Turbulent H_2/Air Premixed Flames

Wonsik Song[a], Francisco E. Hernández Pérez[a], Efstathios-Al. Tingas[b], Hong G. Im[a,*]

[a] *Clean Combustion Research Center (CCRC), King Abdullah University of Science and Technology (KAUST), Thuwal 23955-6900, Saudi Arabia*
[b] *School of Engineering and the Built Environment, Edinburgh Napier University, Edinburgh EH10 5DT, United Kingdom*

Abstract

A statistical analysis is conducted for turbulent hydrogen-air premixed flames at a range of Karlovitz numbers up to 1,126 by direct numerical simulations (DNS) with detailed chemistry. The local and global burning velocities are evaluated and the deviation from the laminar flame speed is assessed. It is found that the global turbulent flame speed is largely determined by the integral length scale than the turbulent Karlovitz number, due to the flame surface area enhancement. The turbulent flame speed in all examined cases correlates well with the flame surface area, according to Damköhler's first hypothesis; even at Karlovitz number well above 1,000, reaction zones stay intact and only the preheat zone is broadened by the strong turbulence level. The statistical analysis with the probability density function (PDF) for the displacement speed shows that the highest probability of the local flame speed coincides with the one-dimensional unstretched flame speed. Despite some deviations, the mean flame structures and reaction rate of hydrogen of the higher Ka cases are found to resemble those of the laminar flame, and this further confirms that the turbulent flame brush topology is mainly determined by the large scale turbulence behavior. The results also suggest that the engineering modeling based on the flamelet concept may be valid for a wider range of Ka conditions.

Keywords: Direct numerical simulation, High Karlovitz number, Turbulent premixed flame, Turbulent flame speed, Turbulent flame structure

---

[*] Corresponding author.
Email address: `hong.im@kaust.edu.sa` (Hong G. Im)

1. Introduction

Computational fluid dynamics (CFD) plays a vital role in the design and development of practical combustion devices. Due to prohibitive computational costs, the device-level simulations rely on Reynolds-averaged Navier–Stokes (RANS) and large eddy simulation (LES) with various mixing and combustion closure/subgrid models. As such, the predictive capability of the simulations depends strongly on the fidelity of the underlying sub-models. For premixed combustion, a common approach is the laminar flamelet concept [1, 2], assuming that the turbulent flame brush is composed of a collection of laminar flamelets that are wrinkled and stretched by the action of turbulent eddies. The modeling framework is implemented, for example, in the form of the flame surface density (FSD) or coherent flame model (CFM) [3, 4].

FSD estimates the mean/filtered chemical source term as the product of the flame surface density (Σ) and the local consumption rate ($\rho_0 \langle S_\mathrm{c} \rangle_s$), where ρ_0 is the unburned gas density and $\langle S_\mathrm{c} \rangle_s$ is the local consumption speed which is further broken down to $S_\mathrm{L}^0 I_s$ with S_L^0 and I_s as the unstretched laminar flame speed and stretch factor, respectively. At typical low Karlovitz numbers ($\mathrm{Ka} < 1$), I_s has been developed by the laminar flame theory. At higher Karlovitz numbers ($1 < \mathrm{Ka} < 100$) in the thin reaction zone regime, the laminar flamelet model may still be applicable by incorporating the enhancement of transport in the preheat zone by turbulent eddies, according to Damköhler's second hypothesis [5]. At $\mathrm{Ka} > 100$, the theoretical "distributed combustion regime" condition is expected, requiring a drastically different reaction closure model to account for a different mode of the strong turbulence-chemistry interaction.

Premixed combustion at high Ka has attracted substantial research interest in recent years as modern combustion devices operate at extreme conditions in pursuit of higher efficiencies. To gain fundamental understanding, laboratory-scale flames at $\mathrm{Ka} > 100$ conditions have been studied experimentally and numerically. Experiments were conducted in swirl [6–10] and pilot [11–15] configurations, while direct numerical simulation (DNS) studies are largely limited to the turbulence-in-a-box configuration, except for a few studies of laboratory-scale combustors [10, 16–21], due to high computational costs. A number of review papers provided a detailed account of recent progress on turbulent premixed combustion research [22–25].

Recent experimental investigations on high Ka turbulent flames mostly focused on flame structures [6, 7, 9, 11, 12, 14]. Wabel et al. [11, 14] proposed a revised turbulent combustion regime diagram by introducing a metric relating the turbulent diffusivity with the molecular one. Zhou et al. [6, 7, 9] measured reactive radicals such as CH and HCO, in addition to CH_2O and OH, which are conventionally used to assess the broadening of preheat or reaction zones. The reaction layers identified by CH and HCO profiles were found to become broadened at high Ka conditions. On the other hand, the scope of DNS studies has been wider by taking advantage of detailed spatially and temporally resolved information, such as the analyses of the turbulent flame speed [24, 26–28], flame structure [29–31], heat release characteristics [32, 33], differential diffusion effects [26, 31, 32, 34–36].

A common conclusion from both experiments and numerical simulations at high Ka conditions is that the preheat zone is broadened considerably by turbulence, whereas the reaction zone stays nearly unaffected or broadened only at significantly high Ka conditions (Ka $\gg$ 1,000) [37]. While many of these studies examined the detailed flame structure in comparison with the reference laminar flames, few studies exist on the statistical analysis of the differences in turbulent burning velocity distributions at low and high Ka conditions, especially for a wide range of the parametric space of the turbulent intensities and integral length scales, which have direct implications in RANS and LES submodels.

Although the turbulent flame speed is affected by both the turbulent intensity (u') and integral length scale (l_T), most of the discussion has focused on the former parameter. The general conclusion for the dependence of the turbulent flame speed (S_T) on u' is that S_T initially increases with u' and becomes saturated at sufficiently large u' as discussed theoretically in [38], numerically in [39], and experimentally in [40], showing the so called "bending effect." The effects of l_T on S_T have so far remained largely unexplored and have been partly investigated in turbulent jet flames [20, 21], spherically expanding flames [41], and turbulence-in-a-box flames [42]. Although these studies commonly reported that S_T has a proportional relation with l_T, the dependence of the stretch factor (defined by $(S_\mathrm{T}/S_\mathrm{L})/(A_\mathrm{T}/A_\mathrm{L})$, with A denoting flame surface area and the subscripts T and L corresponding to the turbulent and laminar counterparts) on the integral length scale was reported to increase in [21] but remained constant in [41, 42]. Moreover, discussion on flame structure over a wide range of parametric spaces is insufficient in the literature despite its importance to turbulent combustion modeling. Hence, for better understanding of turbulent combustion characteristics such as the flame speed and structures, a wide range of the parameters u' and l_{T} should be considered.

To address these issues, the present study investigates the statistical aspects of the local and global turbulent flame speed by using DNS data for turbulent hydrogen-air flames propagating into forced turbulent flows in a periodic box, at a range of Ka conditions (14–1,126) that cover the thin reaction zone and distributed combustion regime. The global turbulent flame speed is directly compared with the surface area growth that is due to the interaction of the flame with turbulent eddies and the effect of the integral length scale on the global flame speed is carefully examined, while local displacement speed is analyzed in a statistical manner and the results are compared with the unstretched laminar flame speed. Finally, the structural changes in the statistical average are evaluated in two different ways: spatially averaged and conditionally averaged against temperature, and modeling implications are discussed.

Table 1: Parameters of the current simulations at $P = 1$ atm, $T_u = 300$ K, and $\phi = 0.7$ under the uniform grid system ($\Delta x = \Delta y = \Delta z$). The Kolmogorov length scale η is evaluated at the unburned condition.

Case	u'/S_{L}	$l_{\mathrm{T}}/\delta_{\mathrm{L}}$	L_y/δ_{L}	η [μm]	Δx [μm]	$\delta_{\mathrm{L}}/\Delta x$	Re	Da	Ka
F1	5	5.65	28.24	14.91	20	17.7	686	1.13	23
F2	35	0.82	4.11	2.14	2.6	136.2	700	0.02	1126
F3	2.6	0.86	4.29	15.15	20	17.7	55	0.33	22
F4	18.3	0.12	0.59	2.14	2.6	136.2	52	0.01	1126
F5	5	0.83	4.16	9.24	11.5	30.8	101	0.17	60
F3$'$	2.6	2.08	10.39	18.90	20	136.2	132	0.80	14
F4$'$	18.3	0.29	1.47	2.67	2.6	17.7	131	0.02	722

2. Numerical method and selected conditions

Direct numerical simulations of propagating flames in a periodic box are carried out using the KAUST Adaptive Reacting Flow Solver (KARFS) [43, 44], which solves the conservation of mass, momentum, energy, and species equations in the compressible formulation by utilizing an eighth-order central-difference scheme for spatial discretization and a fourth-order explicit Runge–Kutta method for the time integration. The nonreflecting Navier–Stokes characteristic boundary conditions (NSCBC) [45, 46] are applied to the outflow boundary of the box configuration, while periodic boundary conditions are applied to the transverse directions.

To initialize the simulations, a one-dimensional premixed flame solution (equivalence ratio $\phi = 0.7$, fresh mixture temperature $T_\mathrm{u} = 300$ K, and pressure $P = 1$ atm) is mapped onto the three-dimensional domain and turbulent velocity fluctuations are superimposed. The initial isotropic turbulence field is generated by specifying the energy spectrum in the spectral space [47] and is further fed at the left boundary $x = 0$. While the turbulent flame propagates to the unburned gas side, the mean inflow velocity is properly adjusted based on the fuel consumption speed, so that the flame is anchored around a specified location within the computational domain, following Bell et al. [48]. To retain the initial turbulence level, the linear turbulent forcing scheme developed in [49] for incompressible flows, is applied in the upstream region starting from 10% of the streamwise domain length. To ensure that the turbulence-flame interaction is realistic, the forcing is turned off as the flow approaches the flame base, defined by a temperature cutoff value of 320 K, which corresponds to the temperature-based progress variable $c_\mathrm{T} \approx 0.01$. Although the cutoff value is somewhat arbitrary, it ensures that the applicability of the forcing scheme remains reasonably valid. It is also noted that the employed turbulent forcing scheme restricts the integral length scale statistically to approximately 1/5 of L_y. The detailed chemical kinetic model by Burke et al. [50] is used, which consists of 9 species and 23 reactions.

For a systematic investigation of the parametric effects at different turbulent combustion regimes, a range of cases have been designed as marked and listed in Fig. 1 and Table 1, respectively. The cases F1 to F4 are located in a parallelogram such that the turbulent Reynolds number (Re) of F1 and F2 is 700, while that of F3 and F4 is 50, yet cases with the same Re have significantly different Karlovitz number (Ka). Fixing the Reynolds number in essence keeps constant the competition between turbulent kinetic energy and the work of the viscous forces. On the other hand, F1 and F3 have the same Ka of approximately 20, while that of F2 and F4 is about 1,126, but cases with the same Ka have significantly different Re. Fixing Ka number essentially fixes the Kolmogorov length scale, therefore, keeping constant the interaction between the flame and the small scale turbulent eddies. To examine the turbulent burning behavior at the same integral length scale l_{T} and different velocity fluctuation levels u', the case F5 is designed such that F3, F5, and F2 are on the same vertical line. Furthermore, to study the scaling of the turbulent flame speed, two extra cases, F3$'$ and F4$'$ were added which have the same u' as F3 and F4, respectively, but larger integral length scales. Note that F3$'$ exhibits the same turbulent combustion characteristics as other cases that fall in the same regime do, hence its general discussion is omitted. Cases F1, F3, F3$'$, and F5 fall into the thin reaction zone regime, while F2, F4, and F4$'$ fall into the distributed combustion regime, according to the Borghi diagram [5].

The relevant nondimensional numbers are expressed as follows:

$$\mathrm{Re} = \frac{u' l_{\mathrm{T}}}{\nu}, \quad \mathrm{Da} = \frac{l_{\mathrm{T}}/u'}{\delta_{\mathrm{L}}/S_{\mathrm{L}}}, \quad \mathrm{Ka} = \frac{\delta_{\mathrm{L}}/S_{\mathrm{L}}}{(\nu/\epsilon)^{1/2}} = \frac{\sqrt{\mathrm{Re}}}{\mathrm{Da}}\,, \tag{1}$$

where u', l_{T}, and ϵ are the root-mean-square turbulent velocity fluctuation, integral length scale of turbulence, and turbulent dissipation rate, respectively, while S_{L}, δ_{L}, and ν refer to the laminar flame speed, laminar thermal thickness, and kinematic viscosity, respectively. The definition of the flame thickness follows the thermal thickness, which is based on the maximum temperature gradient ($\delta_{\mathrm{L}} = (T_{\mathrm{max}} - T_{\mathrm{min}})/(dT/dx)_{\mathrm{max}}$), where T_{max} and T_{min} refer to the maximum and minimum temperature values at the reference one-dimensional laminar premixed flame condition. The values of the laminar flame speed and thermal thickness are 1.356 m/s and 0.354 mm, respectively. The configuration of the simulation is shown in Fig. 2 where L_x, L_y, and L_z are differently chosen such that approximately five integral length scales fit in the L_y and L_z directions for all cases.

Grid resolutions are determined based on the Kolmogorov length scale (η) and satisfy the criterion $\Delta x = \Delta y = \Delta z \leq 2\eta$ [51], with the values for each case listed in Table 1. The time step is determined by the strict condition of the Courant–Friedrichs–Lewy (CFL) number being less than unity. The total number of grid points for F1, F2, F3, F3′, F4, F4′, and F5 are respectively about 250, 516, 1.3, 15.6, 8.2, 52, and 6.3 million, which led to the simulation computing times of approximately 6.1, 6.3, 0.03, 0.39, 0.14, 0.8, and 0.25 million core-hours, respectively, at the KAUST Supercomputing Laboratory.

3. Results and discussion

Figure 2 shows instantaneous snapshots of the temperature field from the various simulations, after the flames reached a fully developed state. The time scale, τ_{eddy}, in the caption is the eddy turnover time defined as $\tau_{\text{eddy}} = l_{\text{T}}/u'$. Fig. 2 clearly shows different responses of the flame front to turbulence depending on the conditions. From the visual inspection, F1 shows the strongest presence of cellular structure on the flame surface, which is attenuated approximately in the order of F5, F3, F2, F4′, and F4. Although the Karlovitz number of F4 is as high as that of F2, F4 resembles a laminar flame without any significant level of corrugation. This may be attributed to three reasons: first, the size of the energy-containing turbulent eddies is too small to wrinkle the flame noticeably; second, the turbulent dissipation rate ($\epsilon \approx u'^3/l_{\text{T}}$) is remarkably high, dissipating the eddies rapidly; and third, the constraints imposed by the size of the lateral and transversal dimensions of the domain. Therefore, when discussing the effects of the integral length scale, F4′ will be used instead of F4. As shown in Fig. 2(d′) and will be discussed later, although F4′ involves a limited domain size in the transversal direction ($L_y/\delta_{\text{L}} \approx 1.5$), turbulent eddies wrinkle the flame front, leading to the expected presence of the turbulence-flame interaction. Nevertheless, readers should be aware of the limitations imposed by the small domain size for F4′, and hence F4′ should be interpreted with caution. Overall, different responses on the flame front suggest that the flame wrinkling has a closer relation with the integral length scale rather than the Karlovitz number alone.

It is thus evident that the size of large scale turbulent eddies is a crucial factor affecting the level of the flame surface corrugation, thereby directly impacting the overall turbulent burning velocity as will be further investigated later. In the following subsections, we will discuss the turbulent burning characteristics in global and local perspectives for different Karlovitz number conditions.

3.1. Turbulent flame speed

Turbulent flame speed as the global burning rate, S_T, is defined by the consumption rate of the fuel species as

$$S_\mathrm{T} = \frac{1}{\rho_\mathrm{u} Y_\mathrm{u,F} A_\mathrm{L}} \int_V \dot{\omega}_\mathrm{F} \, \mathrm{d}V \, , \tag{2}$$

where ρ_u and $Y_\mathrm{u,F}$ are the mixture density and fuel mass fraction, respectively, at the unburned gas side, A_L is the projected flame area onto the direction of the flame propagation, $\dot{\omega}_\mathrm{F}$ is the production rate of the fuel species, and V is the volume of the computational domain.

Figure 3 displays the temporal evolution of the turbulent flame speed and flame surface area for all the cases. The flame surface area was extracted from the iso-surface of the temperature-based progress variable, $c_\mathrm{T} \approx 0.6$, at which the rate of reaction (R1) $\mathrm{H} + \mathrm{O_2} \leftrightarrow \mathrm{O} + \mathrm{OH}$ becomes the maximum in the reference one-dimensional laminar flame. For such a wide range of Karlovitz number, Fig. 3 shows that $S_\mathrm{T}/S_\mathrm{L}$ and $A_\mathrm{T}/A_\mathrm{L}$ are closely correlated for all cases, implying that the Damköhler's first hypothesis ($S_\mathrm{T}/S_\mathrm{L} \sim A_\mathrm{T}/A_\mathrm{L}$) is valid even at Ka conditions that are expected to fall into distributed combustion regime. Moreover, although F1 has a lower turbulence intensity ratio, $u'/S_\mathrm{L} = 5$, compared to F2 (35) and F4$'$ (18.3), the larger integral length scale of F1 ($l_\mathrm{T}/\delta_\mathrm{L} = 5.6$) generates a larger scale wrinkling and larger flame surface area, which in turn enhances the overall turbulent flame speed at a much larger level than that of F2 and F4$'$.

For the case F4$'$ (Fig. 3(d)) with an extremely small integral length scale, the stretch factor $I_0 = (S_\mathrm{T}/S_\mathrm{L})/(A_\mathrm{T}/A_\mathrm{L})$ approaches unity. This may be attributed to the reasons discussed for the case F4 in the early part of the Section 3: the small size of the energy-containing turbulent eddies, large turbulent dissipation rate, ($\epsilon \approx u'^3/l_\mathrm{T}$), and the constraints of the transversal dimensions of the computational domain. Considering that the cases F1 and F3 have the same Ka (20) but present significantly different responses of S_T to A_T, these differences are attributed to the different turbulent Reynolds numbers of 700 (F1) and 50 (F3). Furthermore, the larger length scale ratio of 6.57, in contrast to the RMS velocity ratio of 1.91, between cases F1 and F3 suggests that the integral length scale has a stronger impact on the global turbulent flame speed. Last, by examining the three cases with nearly the same integral length scale but different turbulence intensity (cases F2, F3 and F5), regardless of the Ka (1126, 22 and 60, respectively) and Re (700, 55 and 101, respectively), the turbulent flame speed and surface area are increased by similar factors (around two) as compared to the laminar counterparts.

Although the last result may seem counter-intuitive, it is consistent with the theoretical work of Peters [38], who extended the level-set method to the thin reaction zone regime and showed that as l_{T} decreases, S_{T} becomes less sensitive to u', particularly as $l_{\mathrm{T}}/\delta_{\mathrm{L}}$ approaches one. Considering that for cases F2, F3 and F5, the ratio of length scales $l_{\mathrm{T}}/\delta_{\mathrm{L}} < 1$, it is reasonable to expect a reduced sensitivity of S_{T} to u'. Moreover, according to the technique of Intermittent Turbulent Net Flame Stretch (ITNFS) [52] based on vortex-flame interaction, stretch effects are found to be negligible at small integral length scales and almost independent of u'. This indicates that the efficiency for small scale vortices to wrinkle the flame front is substantially small, thereby the stretch acting on the flame becomes smaller as integral length scales becomes smaller. Overall, these results indicate that the integral length scale is a key parameter dictating the flame surface and global flame speed behavior.

Figure 4 displays the temporally averaged turbulent flame speed and surface area for the time range indicated in Fig. 3 by the horizontal lines, together with the mean stretch factor, $\overline{I_0} = (\overline{S}_{\mathrm{T}}/S_{\mathrm{L}})/(\overline{A}_{\mathrm{T}}/A_{\mathrm{L}})$. In contrast to a large number of studies in the literature, where $S_{\mathrm{T}}/S_{\mathrm{L}}$ has been sought to correlate with either u'/S_{L} or non-dimensional numbers including Re, Da, or Ka, the current result indicates that $S_{\mathrm{T}}/S_{\mathrm{L}}$ and $A_{\mathrm{T}}/A_{\mathrm{L}}$ strongly correlate and proportionally increase with the integral length scale. This is consistent with the previous work by Luca et al. [20] and Attili et al. [21] for a slot jet flame configuration in that $S_{\mathrm{T}}/S_{\mathrm{L}}$ is proportional to $l_{\mathrm{T}}/\delta_{\mathrm{L}}$. In fact, Luca et al. [20] reported that the stretch factor was nearly unity in a global sense, while from a local perspective, Attili et al. [21] suggested that the slight increase of the local I_0 with local $l_{\mathrm{T}}/\delta_{\mathrm{L}}$ involves an extra factor in enhancing the turbulent flame speed, which is the inner layer thickening. A stretch factor of nearly unity was also reported by Lapointe [42] based on DNS data of a turbulence-in-a-box configuration and by Kulkarni et al. [41] for spherically expanding flames with different integral length scales.

Considering that the mean stretch rate ($\overline{I_0}$) is nearly unity for all cases, the flame surface

Table 2: Values of the area ratio ($A_\mathrm{T}/A_\mathrm{L}$), cutoff ratio ($\epsilon_\mathrm{o}/\epsilon_\mathrm{i}$), outer cutoff ($\epsilon_\mathrm{o} = l_\mathrm{T}$), inner cutoff ($\epsilon_\mathrm{i} = \nu/S_\mathrm{L}$), and fractal dimension (D_f).

Case	$A_\mathrm{T}/A_\mathrm{L}$	$\epsilon_\mathrm{o}/\epsilon_\mathrm{i}$	ϵ_o [m]	ϵ_i [m]	D_f
F1	5.855	137.316	2.001×10^{-3}	1.457×10^{-5}	2.359
F2	1.863	19.929	2.904×10^{-4}	1.457×10^{-5}	2.208
F3	1.821	20.901	3.045×10^{-4}	1.457×10^{-5}	2.197
F4	1.002	2.916	4.249×10^{-5}	1.457×10^{-5}	2.002
F5	1.982	20.172	2.939×10^{-4}	1.457×10^{-5}	2.228
F3′	3.330	50.527	7.362×10^{-4}	1.457×10^{-5}	2.307
F4′	1.041	7.145	1.041×10^{-4}	1.457×10^{-5}	2.021

area, and thereby S_T, can be estimated as represented by the fractal theory [53, 54]: $A_\mathrm{T}/A_\mathrm{L} = (\epsilon_\mathrm{o}/\epsilon_\mathrm{i})^{D_f-2}$, where ϵ_o and ϵ_i are the outer and inner cutoff scales, respectively, and D_f is the fractal dimension. In the current study, D_f is found to be between 2 and 2.36 with the outer and inner cutoff scales taken as the integral length scale and nominal laminar flame thickness ($l_f = \nu/S_\mathrm{L}$), respectively. In Table 2, the values of the area ratio, cutoff ratio, outer cutoff, inner cutoff, and fractal dimension are all listed. Except for the cases of F4 and F4′, which have extremely small integral length scales and are deemed unimportant for practical conditions, D_f is between 2.20 and 2.36, which is consistent with the previous studies summarized in [5, 53, 54]. Through the fractal theory relation for $A_\mathrm{T}/A_\mathrm{L}$ with $\epsilon_\mathrm{o} = l_\mathrm{T}$, the predominant role of the integral length scale in the generation of flame surface and magnitude of the turbulent flame speed is further substantiated.

3.2. Displacement speed

In this section, more detailed local turbulence-chemistry interaction characteristics are analyzed in terms of the flame displacement speed, which is defined as the local flame front speed relative to the flow velocity, evaluated based on a species k. In the density-weighted form [55], it is expressed as

$$S_\mathrm{d}^* = \frac{\rho S_\mathrm{d}}{\rho_\mathrm{u}} = \frac{1}{\rho_\mathrm{u}|\nabla Y_k|}\left[\dot{\omega}_k - \nabla\cdot\mathbf{J}_k\right], \tag{3}$$

where ρ, $|\nabla Y_k|$, $\dot{\omega}_k$, and $\nabla \cdot \mathbf{J}_k$ are the mixture density, absolute value of the mass fraction gradient, net production rate, and diffusion rate of a species k, respectively. The subscript u refers to the unburned state. The diffusive term has the form $\nabla \cdot \mathbf{J}_k = -\nabla \cdot \big(\rho D_k \nabla Y\big)$, with D_k being the mixture-averaged diffusion coefficient of the species k. The density-weighting eliminates the inherent effect of the velocity acceleration through the flame due to thermal expansion. In the current study, S_d^* is computed based on the fuel species ($\mathrm{H_2}$).

To illustrate the variation of S_d^* and other key solution variables across the flame front, two-dimensional (2D) cuts are presented in Fig. 5, including the heat release rate (HRR), temperature (T), mass fraction of $\mathrm{H_2}$ (Y_H2), mass fraction of $\mathrm{H_2O_2}$ (Y_H2O2), and mass fraction of OH (Y_OH) at the time instant shown in Fig. 2. Note that case F4′ was excluded from Fig. 5 due to exhibiting relatively minor wrinkling. The gray lines indicate the isocontours of the progress variable (c_T) from 0.1 to 0.7 with an increment of 0.2 for F1 and 0.1 for the rest. The complex structures in the rectangular regions in F1 are magnified in the inset.

Comparing the cases on the same scale of the domain indicates that the averaged normal distance between $c_\mathrm{T} = 0.1$ and 0.7 is comparable for F1, F3, and F5 while it becomes more blurred and thickened for F2, which is mainly due to the increased level of corrugations in the upstream, for example, isolevels $0.1 < c_\mathrm{T} < 0.4$. Comparing F1 with F2, case F1 involves larger Kolmogorov scale eddies which cannot perturb the flame, while in F2, substantially smaller turbulent eddies disrupt the flame structure, as seen by the large variations in the temperature layer thickness. For the larger turbulence scales of F1, the flame front exhibits a higher level of wrinkling, which is attributed not only to a wider range of eddies interacting with flame front, but also to a stronger level of thermodiffusive imbalance, as discussed earlier in [56–58], in which the large corrugation of the flame front was only observed when the thermodiffusive instability was pronounced. Comparing F2, F3, and F5 which have the same integral length scale, the level of wrinkling shown in HRR and Y_OH looks similar for these cases. However, turbulence in F2 with a much higher u' than that in F3 and F5 interacts with the flame strongly as evidenced by T and Y_H2O2, particularly in the upstream region. Finally, although not shown here, but implied in Fig. 2(d′), F4′ with a substantially small integral length scale exhibits a less wrinkled flame, despite Ka being 712. Again, this suggests that the integral length scale plays a key role in dictating the turbulent flame topology, while Ka based on the Kolmogorov eddy scale is limited to the highly localized flame characteristics.

For S_d^* distribution shown on the top row in Fig. 5, conditioned for $0.01 < c_\mathrm{T} < 0.99$ and set to zero outside where the flame is undefined, F1, F3, and F5 show more uniform distributions along the wrinkled flame fronts as compared to F2. In F2, S_d^* fluctuates largely due to stronger and more localized turbulence-chemistry interaction. The high turbulence intensity in F2 results in a significantly larger distortion of the upstream layers of the flame front, but still the reaction zone remains intact. This is evident by the progress variable isocontours greater than 0.3 that are nearly parallel with one another. The temperature starts to rise in the more upstream region than the actual region of heat release due to the disruption of the flame front by turbulence, which, at the same time, enhances the dissipation by viscous effects (see the profiles of HRR and T in Fig. 5). Moreover, this intense turbulence-chemistry interaction and front disruption are clearly manifested in the broadened Y_H2O2 distribution that spreads upstream, yet the distribution of Y_OH nearly coincides with that of the heat release rate. In summary, F2 at Ka $>$ 1,000 clearly shows different flame structures with much broader and disrupted transport zones. Even so, due to the thermal expansion in the region, the small scale eddies are dissipated by the time they reach the reaction zones, and hence the theoretical “distributed combustion” regime is not realized. This finding is consistent with previous experimental and computational studies [11, 13–15, 30].

As a statistical analysis, the probability density functions (PDF) of S_d^* are computed and displayed in Fig. 6 where (a) to (e) correspond to cases F1 to F5, respectively. S_d^* was computed by collecting data over multiple time steps after the turbulent flame was fully developed. Hence, 17, 33, 54, 65, and 79 data sets were utilized for the cases F1 to F5, respectively, corresponding to all eddy turnover times within the horizontal lines in Fig. 3. Two isocontour values, $c_\mathrm{T} = 0.2$ (blue) and 0.6 (red), are chosen to represent the preheat and reaction zones, respectively. These values are selected because in the reference laminar premixed flame $c_\mathrm{T} = 0.2$ is where $\dot{\omega}_{\mathrm{H_2O_2}}$ crosses from negative to positive, and $c_\mathrm{T} = 0.6$ is the point at which the reaction rate of $\mathrm{R1{=}H{+}O_2 \leftrightarrow O{+}OH}$ reaches its maximum. The dashed lines are associated with the S_d^* values obtained from the reference laminar premixed flame solution for each selected c_T value.

As seen from Fig. 6, the highest probability of S_d^* is found to closely match the S_d^* value of the reference laminar flame. This implies that for all Ka conditions considered in the current study, the majority of the flame components burn as the laminar flame. Moreover, although the global turbulent flame speed is higher in F1 (see Fig. 3) due to the growth of the flame surface area, the local front speed does not follow this trend. As expected from Fig. 5, the distribution of S_d^* for F2 (Fig. 6(b)) spans most widely to both negative and positive sides, followed by the F4$'$, F5, and F3 ($\sim$F1) - with the order of Ka. Although F5 in Fig. 6(e) shows a relatively strong motion of turbulent eddies at the preheat region evident by the fact that a negative distribution of S_d^* exists, turbulence is attenuated downstream and the PDF shifts to positive values of S_d^* (red line). This behavior is more pronounced in the cases F1 and F3 where practically no negative distribution of S_d^* exists. For F4$'$ with the same u' as F4 but larger l_T, unlike F4 in which S_d^* is strongly localized at the laminar flame speed, local stretch effects are evident, showing a similar distribution to F2.

The trend of the front speed as a function of the turbulent intensity is consistent with the previous work by Nivarti and Cant in a turbulence-in-a-box configuration [39] in that at a relatively smaller turbulence level, the distribution of the PDF is narrower and more localized, but as the turbulent intensity increases, the distribution of the PDF is extended to the negative side. The most probable front speed reported in [39] was far from S_L, which is expected considering that it was density unweighted. In summary, the results of front speed confirm that the global flame speed may be largely different from the local speed which is strongly affected by the local stretch effects.

Figure 7 shows the variance and skewness of S_d^* based on data collected for the time period indicated by the horizontal lines in Fig. 3. The same color convention is applied: blue (diamond symbol) and red (triangle symbol) colors indicate the upstream and downstream regions, defined by the progress variable $c_\mathrm{T} = 0.2$ and 0.6, respectively. Figs. 7(a) and (b) present the variance and skewness plotted against $l_\mathrm{T}/\delta_\mathrm{L}$, while in (c) and (d) they are plotted against u'/S_L. Although a clear trend was not observed for both parameters, the variance appears to be rather correlated with u' than with l_T, whereas the skewness is rather correlated with l_T than with u'. Moreover, the variance becomes smaller downstream due to the decay of turbulence, but the skewness becomes larger downstream, indicating that a faster speed is more probable there. A noticeable observation is the large variance of cases F2 and F4′ due to the strong motion of turbulence in the upstream region, which clearly shows a small value of skewness (i.e., nearly symmetric) for F4′ and even a negative value of skewness for F2.

3.3. Turbulent flame structure

In the following, we discuss the global flame structure from two different perspectives: one via cross-sectional averaging and the other via conditional averaging. While the cross-sectional averaging would be more realistic since it accounts for situations of unburned pockets moving through the burned gas, it may not be entirely intuitive as will be discussed below. On the other hand, by conditionally averaging, all mass fractions and temperature are conditioned on each "bin" of the progress variable, hence the structures are expected to be more similar among the cases.

3.3.1. Cross-sectional averaged structure

Figures 8 and 9 respectively show the temporal average of the cross-section means of temperature along with major species, and intermediate species for cases F1–F5. To facilitate the comparison among all the turbulent cases and contrast them with the laminar one, the profiles are plotted as a function of the progress variable $c_{\bar{T}}$, which is computed using the temporally and spatially averaged temperature field for each turbulent case. Data from the DNS are represented by the solid lines (mean) and shaded regions (standard deviation about the mean), while the laminar counterparts are marked by dashed lines. All species mass fractions and the temperature of DNS data are normalized by the maximum value of the corresponding variable in the reference laminar premixed flame solution.

Starting from F4′ in Fig. 8(d), the mean values of all major species and temperature profiles closely follow the laminar ones, despite exhibiting fluctuations caused by the effects of turbulence, even for the sufficiently large $\mathrm{Ka} > 700$. As discussed earlier, this laminar-like flame structure is attributed to the large dissipation rate of turbulent kinetic energy as well as the small size of the energy containing eddies, which are dissipated rapidly. On the other hand, for all the other cases with larger integral length scales, deviations from the laminar profiles are observed in all major species and temperature, which are also accompanied by significant levels of fluctuations, as indicated by the wider shaded areas. This is especially true for the fuel species H_2, whose profiles substantially differ from the laminar one, while T and all other species of O_2, and H_2O are found to be closer to their laminar counterparts.

The deviation of the turbulent flame structure from the laminar one at different integral length scale is more pronounced in the profiles of the intermediate species. For example, in Fig. 9(a), corresponding to F1 with the largest integral length scale, not only are the peaks of H, O, HO_2, and H_2O_2 much smaller than the laminar counterparts but also the location of the peak is shifted for HO_2 and H_2O_2 to further downstream. For F2, F3, and F5 having the same integral length scale, the mean distributions and peak locations of H, O, and OH are closer to the laminar ones, and the peaks of HO_2 and H_2O_2 are not as much shifted as in F1, yet their values are still significantly smaller. As expected, for F4$'$ with further diminished integral length scale but a large enough $\mathrm{Ka} > 700$, the HO_2 and H_2O_2 profiles noticeably approach the laminar ones and, despite some deviations, other intermediate species also follow the laminar ones. It is clear that the turbulent flame structures in terms of all major and minor species concentrations are also largely affected by the integral length scales.

3.3.2. Conditionally averaged structure

Figures 10 and 11 display the conditionally averaged temperature and major species, and intermediate species, respectively. The notation is the same as in the cross-sectional averaging: solid lines and shaded regions are the mean and standard deviation, and the dashed lines are quantities obtained from the reference laminar flame. As shown in Fig. 10, in addition to F4$'$ in Fig. 10(d) having the small integral length scale and its mean mass fractions and temperature matching well with the corresponding laminar's counterparts in the spatial averaging, all other cases exhibit a marked resemblance between laminar and DNS values for most quantities, except for the mass fraction of H_2. The trend of the mass fraction of H_2 deviating more from the laminar profile is attributed to preferential diffusion, which is affected by the local level of curvature as well. It is also noted that the deviations in H_2 from the laminar profile are more pronounced for F2, F3 and F5, which correspond to $\mathrm{Da} < 1$, i.e., when turbulent transport is faster than chemistry.

Figure 11 shows the conditional average of the intermediate species of DNS together with the reference laminar flame. It also indicates clearly that the conditionally averaged mass fractions follow closer the laminar counterparts, compared to the spatially averaged ones. Moreover, there are noticeable features among the cases. First, as expected by the 2D slice figures (Fig. 5) for the case F2, the spreading of $Y_{\mathrm{H_2O_2}}$ is significant, which may result in displacement of the peaks of $Y_{\mathrm{HO_2}}$ and $Y_{\mathrm{H_2O_2}}$. In addition, the conversion between the two species is not as efficient as in other cases, which is evident by the much lower peak of $Y_{\mathrm{H_2O_2}}$ compared to that in the other cases. Second, Y_{H} of F1 develops much earlier than in other cases, and its peak is found further upstream. This is associated with preferential diffusion, which is a characteristic feature of the light species $\mathrm{H_2}$ and H and its effects are manifested in the thermodiffusive instability.

So far we have demonstrated that the integral length scale is a key factor that determines the global behavior of turbulent premixed flames including the turbulent flame speed and turbulent flame structure. To further examine the effect of the integral length scale on the statistical structure of the fuel consumption rate, the cross-sectional and conditional averaged distribution of the reaction rate of $\mathrm{H_2}$ for F1–F5 is compared against that of the reference laminar flame, as shown in Fig. 12. Note that the curves for different cases are not to scale with one another because the net flame brush thickness is different. For the cross-sectional averaging in Fig. 12(a), qualitatively, F4$'$ follows the laminar flame profile closely because of the small integral length scale, while all other cases show the parabolic shape that is typical of a turbulent flame brush consisting of highly corrugated laminar flamelets. The fact that all cases F1-F3 and F5, except for F4$'$, show the parabolic behavior regardless of the Ka condition, further confirms that the turbulent flame topology and burning characteristics are highly dictated by the integral length scale rather than the smallest turbulent eddies. For the conditional averaging, all the cases qualitatively follow the laminar profile, differing quantitatively in the location and magnitude of their peaks, with the latter being larger. Although the case F4$'$ is the closest to the laminar one, it is again emphasized that this case is subject to limitations imposed by the small domain size ($L_y/\delta_{\mathrm{L}} \approx 1.5$) and should be interpreted with caution.

In the flamelet modeling framework, the chemical composition is typically determined via the tabulation of chemistry, which is essentially the chemical state conditioned on the progress variable. Recently, Lipatnikov et al. [59] assessed the flamelet prediction capability of major and intermediate species, reaction rates, and heat release rate for turbulent hydrogen flames located in different turbulent combustion regimes. The prediction with PDF suggested that the major species were well predicted even for their highest Karlovitz number ($\mathrm{Ka} = 126$), while the predictions of intermediate species and reaction rate of H_2 were less accurate. Consistent with [59], in the current study the conditional averages on the progress variable c suggest that the flamelet assumption for tabulation of major species may still be applicable for $\mathrm{Ka} > 100$, while limited accuracy may exist for intermediate species and the reaction rate of H_2. Since H_2 exhibits preferential diffusion, a H_2-based progress variable is recommended.

4. Conclusions

Direct numerical simulations of turbulent hydrogen-air premixed flames in a periodic box configuration were used to investigate the turbulent flame speed and statistical characteristics of various flamelet quantities at a wide range of Karlovitz numbers. While the number of cases is limited, the seven cases under consideration systematically cover the parametric conditions to explore the effects at a fixed Ka, integral length scale, and turbulence intensity. Whereas the conceptual understanding of high Ka involves more turbulence-chemistry interaction, the statistical analyses of the displacement speed demonstrate that the overall flame behavior at Ka as large as 1,000 still shows remarkable resemblance to that of a laminar flame. Moreover, instead of the non-dimensional numbers such as Re or Ka, the integral length scale plays a vital role in dictating the global characteristics of turbulent premixed flames. Some key findings are summarized as:

1. The turbulent flame speed is closely linked to the integral length scale.
2. The most probable S_d^* coincides with the value computed at the 1D reference laminar condition.
3. Even at high Ka well above 1,000, the reaction zone stays intact due to the decay of turbulence, and only the preheat zone is strongly affected by turbulence.

4. The cross-sectional averages of the temperature and major species appear to be within an acceptable range in comparison with those of the laminar flame, suggesting that the laminar flamelet assumption may be applicable for the cases considered in the current study. However, the distributions of intermediate species and fuel reaction rate are more sensitive to variations in the integral length scale: larger (smaller) integral length scales resulted in more (less) deviation from the 1D reference flame.

5. The conditional averages indicate that the deviation of the flame structures and reaction rate of the fuel species between DNS and the laminar flame appears to be small. Nevertheless, the averaged structure of H_2 is found to be least matched with that of the laminar flame due to different levels of thermodiffusive effects depending on the case.

The results suggest that the formation of different levels of the turbulent flame brush is largely determined by the integral eddy scale relative to the flame thickness combined with a large spectrum of scale, not solely by the Karlovitz number. Although similar findings have been reported in the past, the effect of the integral length scale relative to the flame thickness has been largely overlooked in previous studies, mainly due to the prohibitive computational cost, and how the present findings extend at flames at much larger physical scales demands further investigation.

Acknowledgments

This work was sponsored by King Abdullah University of Science and Technology (KAUST). Computational resources were provided by the KAUST Supercomputing Laboratory (KSL). The work of EAT was also supported by the Royal Society of Edinburgh (RSE) through the RSE/Scottish Government Sabbatical Research Grant scheme with grant no. 64676.

References

[1] N. Peters, Laminar flamelet concepts in turbulent combustion, Symp. (Int.) Combust. 21 (1) (1988) 1231–1250.

[2] T. Poinsot, D. Veynante, Theoretical and numerical combustion, RT Edwards, Inc., 2005.

[3] F. E. Marble, J. E. Broadwell, The coherent flame model for turbulent chemical reactions, Tech. rep., Purdue University Lafayette in Project SQUIDHEADQUARTERS (1977).

[4] A. Trouvé, T. Poinsot, The evolution equation for the flame surface density in turbulent premixed combustion, J. Fluid Mech. 278 (1994) 1–31.

[5] N. Peters, Turbulent combustion, Cambridge university press, 2000.

[6] B. Zhou, C. Brackmann, Z. Li, M. Aldén, X.-S. Bai, Simultaneous multi-species and temperature visualization of premixed flames in the distributed reaction zone regime, Proc. Combust. Inst. 35 (2) (2015) 1409–1416.

[7] B. Zhou, C. Brackmann, Q. Li, Z. Wang, P. Petersson, Z. Li, M. Aldén, X.-S. Bai, Distributed reactions in highly turbulent premixed methane/air flames: Part I. flame structure characterization, Combust. Flame 162 (7) (2015) 2937–2953.

[8] B. Zhou, Q. Li, Y. He, P. Petersson, Z. Li, M. Aldén, X.-S. Bai, Visualization of multiregime turbulent combustion in swirl-stabilized lean premixed flames, Combust. Flame 162 (7) (2015) 2954–2958.

[9] B. Zhou, C. Brackmann, Z. Wang, Z. Li, M. Richter, M. Aldén, X.-S. Bai, Thin reaction zone and distributed reaction zone regimes in turbulent premixed methane/air flames: Scalar distributions and correlations, Combust. Flame 175 (2017) 220–236.

[10] Z. Wang, B. Zhou, S. Yu, C. Brackmann, Z. Li, M. Richter, M. Aldén, X.-S. Bai, Structure and burning velocity of turbulent premixed methane/air jet flames in thin-reaction zone and distributed reaction zone regimes, Proc. Combust. Inst. 37 (2) (2019) 2537–2544.

[11] T. M. Wabel, A. W. Skiba, J. E. Temme, J. F. Driscoll, Measurements to determine the regimes of premixed flames in extreme turbulence, Proc. Combust. Inst. 36 (2) (2017) 1809–1816.

[12] T. M. Wabel, A. W. Skiba, J. F. Driscoll, Turbulent burning velocity measurements: Extended to extreme levels of turbulence, Proc. Combust. Inst. 36 (2) (2017) 1801–1808.

[13] T. M. Wabel, A. W. Skiba, J. F. Driscoll, Evolution of turbulence through a broadened preheat zone in a premixed piloted bunsen flame from conditionally-averaged velocity measurements, Combust. Flame 188 (2018) 13–27.

[14] A. W. Skiba, T. M. Wabel, C. D. Carter, S. D. Hammack, J. E. Temme, J. F. Driscoll, Premixed flames subjected to extreme levels of turbulence part I: Flame structure and a new measured regime diagram, Combust. Flame 189 (2018) 407–432.

[15] A. W. Skiba, C. D. Carter, S. D. Hammack, J. D. Miller, J. R. Gord, J. F. Driscoll, The influence of large eddies on the structure of turbulent premixed flames characterized with stereo-PIV and multi-species PLIF at 20 khz, Proc. Combust. Inst. 37 (2) (2019) 2477–2484.

[16] H. Wang, E. R. Hawkes, J. H. Chen, Turbulence-flame interactions in DNS of a laboratory high Karlovitz premixed turbulent jet flame, Phys. Fluids 28 (9) (2016) 095107.

[17] H. Wang, E. R. Hawkes, B. Zhou, J. H. Chen, Z. Li, M. Aldén, A comparison between direct numerical simulation and experiment of the turbulent burning velocity-related statistics in a turbulent methane-air premixed jet flame at high Karlovitz number, Proc. Combust. Inst. 36 (2) (2017) 2045–2053.

[18] H. Wang, E. R. Hawkes, J. H. Chen, A direct numerical simulation study of flame structure and stabilization of an experimental high Ka CH4/air premixed jet flame, Combust. Flame 180 (2017) 110–123.

[19] H. Wang, E. R. Hawkes, B. Savard, J. H. Chen, Direct numerical simulation of a high Ka CH4/air stratified premixed jet flame, Combust. Flame 193 (2018) 229–245.

[20] S. Luca, A. Attili, E. L. Schiavo, F. Creta, F. Bisetti, On the statistics of flame stretch in turbulent premixed jet flames in the thin reaction zone regime at varying Reynolds number, Proc. Combust. Inst. 37 (2) (2019) 2451–2459.

[21] A. Attili, S. Luca, D. Denker, F. Bisetti, H. Pitsch, Turbulent flame speed and reaction layer thickening in premixed jet flames at constant Karlovitz and increasing Reynolds numbers, arXiv preprint arXiv:2005.04040 (2020).

[22] A. Lipatnikov, J. Chomiak, Turbulent flame speed and thickness: phenomenology, evaluation, and application in multi-dimensional simulations, Prog. Energy Combust. Sci. 28 (1) (2002) 1–74.

[23] J. F. Driscoll, Turbulent premixed combustion: Flamelet structure and its effect on turbulent burning velocities, Prog. Energy Combust. Sci. 34 (1) (2008) 91–134.

[24] H. G. Im, P. G. Arias, S. Chaudhuri, H. A. Uranakara, Direct numerical simulations of statistically stationary turbulent premixed flames, Combust. Sci. Technol. 188 (8) (2016) 1182–98.

[25] J. F. Driscoll, J. H. Chen, A. W. Skiba, C. D. Carter, E. R. Hawkes, H. Wang, Premixed flames subjected to extreme turbulence: Some questions and recent answers, Prog. Energy Combust. Sci. 76 (2020) 100802.

[26] A. Aspden, M. Day, J. Bell, Turbulence–flame interactions in lean premixed hydrogen: transition to the distributed burning regime, J. Fluid Mech. 680 (2011) 287–320.

[27] S. Lapointe, G. Blanquart, Fuel and chemistry effects in high Karlovitz premixed turbulent flames, Combust. Flame 167 (2016) 294–307.

[28] H. A. Uranakara, S. Chaudhuri, H. L. Dave, P. G. Arias, H. G. Im, A flame particle tracking analysis of turbulence–chemistry interaction in hydrogen–air premixed flames, Combust. Flame 163 (2016) 220–240.

[29] H. Carlsson, R. Yu, X.-S. Bai, Flame structure analysis for categorization of lean premixed CH4/air and H2/air flames at high Karlovitz numbers: direct numerical simulation studies, Proc. Combust. Inst. 35 (2) (2015) 1425–1432.

[30] B. Savard, B. Bobbitt, G. Blanquart, Structure of a high Karlovitz n-C7H16 premixed turbulent flame, Proc. Combust. Inst. 35 (2) (2015) 1377–1384.

[31] B. Savard, G. Blanquart, Broken reaction zone and differential diffusion effects in high Karlovitz n-C7H16 premixed turbulent flames, Combust. Flame 162 (5) (2015) 2020–2033.

[32] H. Carlsson, R. Yu, X.-S. Bai, Direct numerical simulation of lean premixed CH4/air and H2/air flames at high Karlovitz numbers, Int. J. Hydrogen Energy 39 (35) (2014) 20216–20232.

[33] A. Aspden, M. Day, J. Bell, Turbulence-chemistry interaction in lean premixed hydrogen combustion, Proc. Combust. Inst. 35 (2) (2015) 1321–1329.

[34] A. Aspden, M. Day, J. Bell, Characterization of low Lewis number flames, Proc. Combust. Inst. 33 (1) (2011) 1463–1471.

[35] A. Aspden, M. Day, J. Bell, Lewis number effects in distributed flames, Proc. Combust. Inst. 33 (1) (2011) 1473–1480.

[36] S. Lapointe, B. Savard, G. Blanquart, Differential diffusion effects, distributed burning, and local extinctions in high Karlovitz premixed flames, Combust. Flame 162 (9) (2015) 3341–3355.

[37] A. Aspden, M. Day, J. Bell, Towards the distributed burning regime in turbulent premixed flames, arXiv preprint arXiv:1806.09865 (2018).

[38] N. Peters, The turbulent burning velocity for large-scale and small-scale turbulence, J. Fluid Mech. 384 (1999) 107–132.

[39] G. Nivarti, S. Cant, Direct numerical simulation of the bending effect in turbulent premixed flames, Proc. Combust. Inst. 36 (2) (2017) 1903–1910.

[40] R. Abdel-Gayed, D. Bradley, M. Lawes, Turbulent burning velocities: a general correlation in terms of straining rates, Proc. R. Soc. Lond. A 414 (1847) (1987) 389–413.

[41] T. Kulkarni, R. Buttay, M. H. Kasbaoui, A. Attili, F. Bisetti, Reynolds number scaling of burning rates in spherical turbulent premixed flames, J. Fluid Mech. 906 (2020).

[42] S. Lapointe, Simulation of premixed hydrocarbon flames at high turbulence intensities, Ph.D. thesis, California Institute of Technology (2016).

[43] F. E. Hernández Pérez, N. Mukhadiyev, X. Xu, A. Sow, B. J. Lee, R. Sankaran, H. G. Im, Direct numerical simulations of reacting flows with detailed chemistry using many-core/GPU acceleration, Comput. Fluids 173 (2018) 73–79.

[44] S. Desai, Y. J. Kim, W. Song, M. B. Luong, F. E. Hernández Pérez, R. Sankaran, H. G. Im, Direct numerical simulations of turbulent reacting flows with shock waves and stiff chemistry using many-core/GPU acceleration, Comput. Fluids 215 (2020) 104787.

[45] C. S. Yoo, Y. Wang, A. Trouvé, H. G. Im, Characteristic boundary conditions for direct simulations of turbulent counterflow flames, Combust. Theory Model. 9 (4) (2005) 617–646.

[46] C. S. Yoo, H. G. Im, Characteristic boundary conditions for simulations of compressible reacting flows with multi-dimensional, viscous and reaction effects, Combust. Theory Model. 11 (2) (2007) 259–286.

[47] T. Passot, A. Pouquet, Numerical simulation of compressible homogeneous flows in the turbulent regime, J. Fluid Mech. 181 (1987) 441–466.

[48] J. Bell, M. Day, J. Grcar, M. Lijewski, Active control for statistically stationary turbulent premixed flame simulations, Comm. Appl. Math. Comp. Sci. 1 (1) (2007) 29–51.

[49] M. Bassenne, J. Urzay, G. I. Park, P. Moin, Constant-energetics physical-space forcing methods for improved convergence to homogeneous-isotropic turbulence with application to particle-laden flows, Phys. Fluids 28 (3) (2016) 035114.

[50] M. P. Burke, M. Chaos, Y. Ju, F. L. Dryer, S. J. Klippenstein, Comprehensive H2/O2 kinetic model for high-pressure combustion, Int. J. Chem. Kinet. 44 (7) (2012) 444–474.

[51] S. B. Pope, Turbulent flows (2001).

[52] C. Meneveau, T. Poinsot, Stretching and quenching of flamelets in premixed turbulent combustion, Combust. Flame 86 (4) (1991) 311–332.

[53] F. C. Gouldin, An application of fractals to modeling premixed turbulent flames, Combust. Flame 68 (3) (1987) 249–266.

[54] Ö. L. Gülder, Turbulent premixed combustion modelling using fractal geometry, Symp. (Int.) Combust. 23 (1) (1991) 835–842.

[55] H. G. Im, J. H. Chen, Structure and propagation of triple flames in partially premixed hydrogen–air mixtures, Combust. Flame 119 (4) (1999) 436–454.

[56] R. Yu, X.-S. Bai, V. Bychkov, Fractal flame structure due to the hydrodynamic Darrieus-Landau instability, Phys. Rev. E 92 (6) (2015) 063028.

[57] C. E. Frouzakis, N. Fogla, A. G. Tomboulides, C. Altantzis, M. Matalon, Numerical study of unstable hydrogen/air flames: shape and propagation speed, Proc. Combust. Inst. 35 (1) (2015) 1087–1095.

[58] L. Berger, K. Kleinheinz, A. Attili, H. Pitsch, Characteristic patterns of thermodiffusively unstable premixed lean hydrogen flames, Proc. Combust. Inst. 37 (2) (2019) 1879–1886.

[59] A. N. Lipatnikov, V. A. Sabelnikov, F. E. Hernández-Pérez, W. Song, H. G. Im, A priori DNS study of applicability of flamelet concept to predicting mean concentrations of species in turbulent premixed flames at various Karlovitz numbers, Combust. Flame 222 (2020) 370–382.

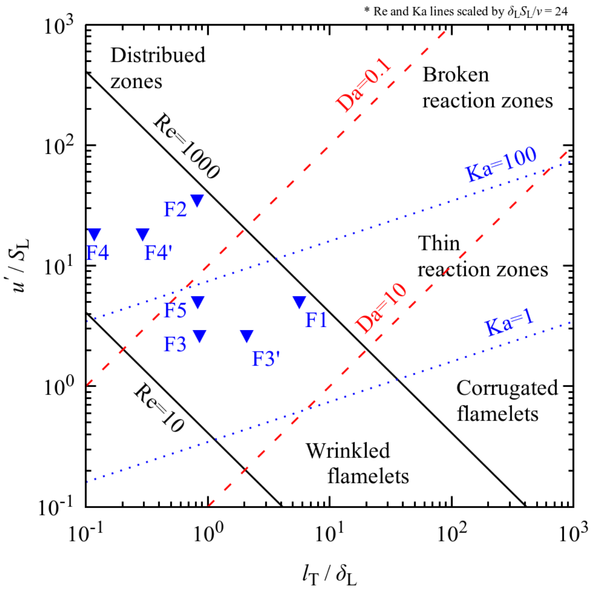

Figure 1: Simulation conditions on the Borghi-Peters diagram. F1 to F4 are in the parallelogram, while F5 has the same l_T as F2 and F3 and the same u' as F1. F3′ and F4′ denote the same u' as F3 and F4, respectively, but larger l_T.

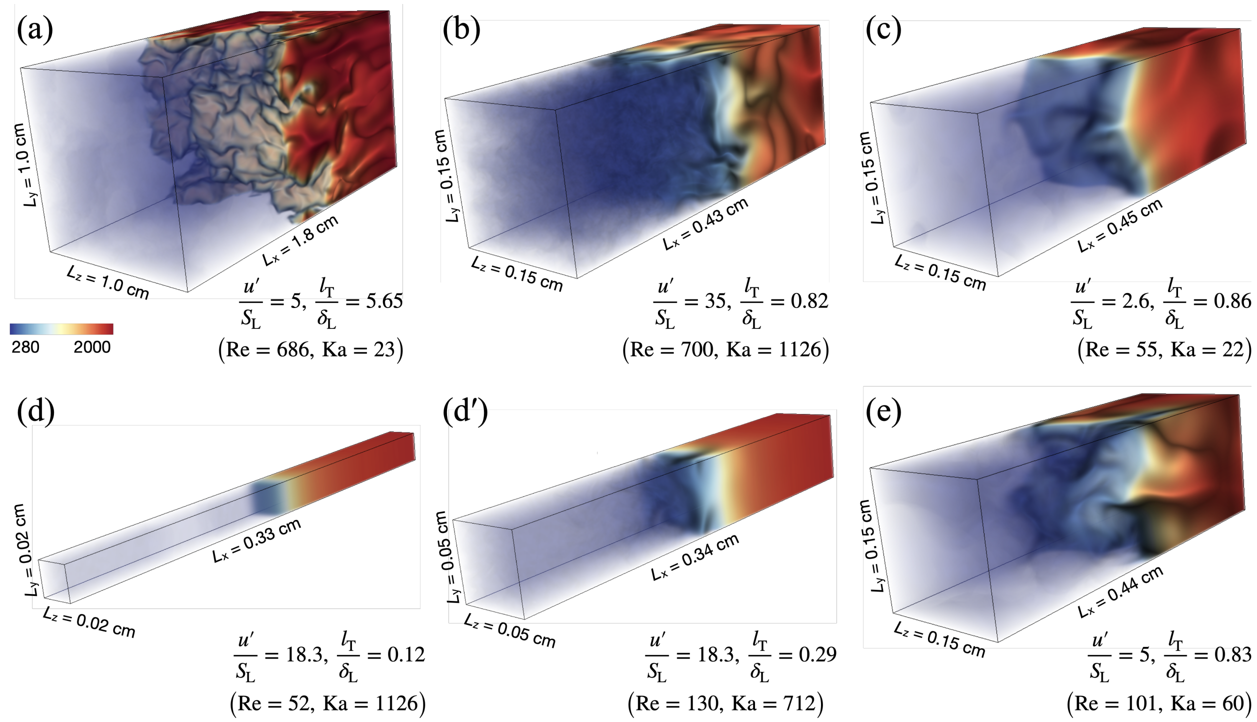

Figure 2: Configurations of the computational domain for flames (a) F1, (b) F2, (c) F3, (d) F4, (d′) F4′, and (e) F5. Shown figures are the temperature at the time step t/τ_{eddy} = (a) 19, (b) 53, (c) 65, (d) 182, (d′) 65, and (e) 95.

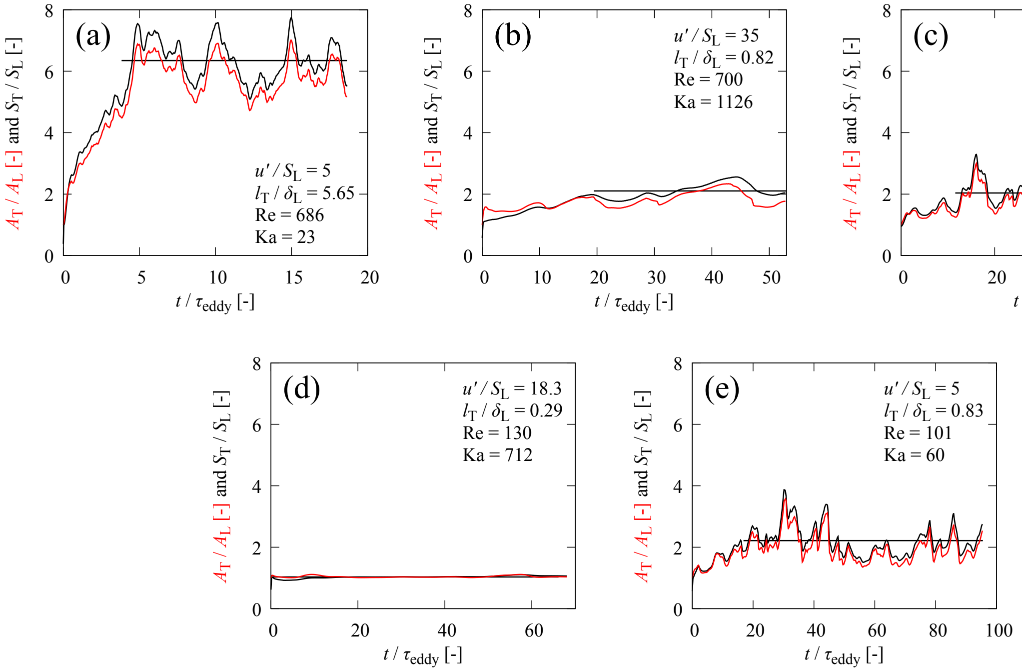

Figure 3: Temporal evolution of the turbulent flame speed and the flame surface area divided by the corresponding laminar quantity for (a) F1, (b) F2, (c) F3, (d) F4′, and (e) F5. The horizontal lines denote the mean turbulent flame speed computed for the shown period of time, truncating the initial transient period.

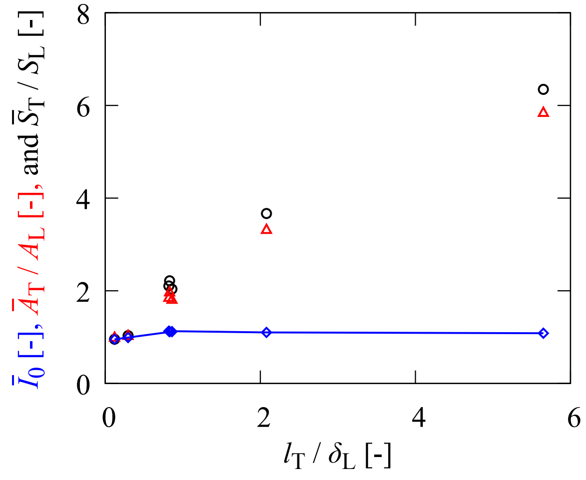

Figure 4: Scaling of the mean turbulent flame speed and mean flame surface area against the integral length scale.

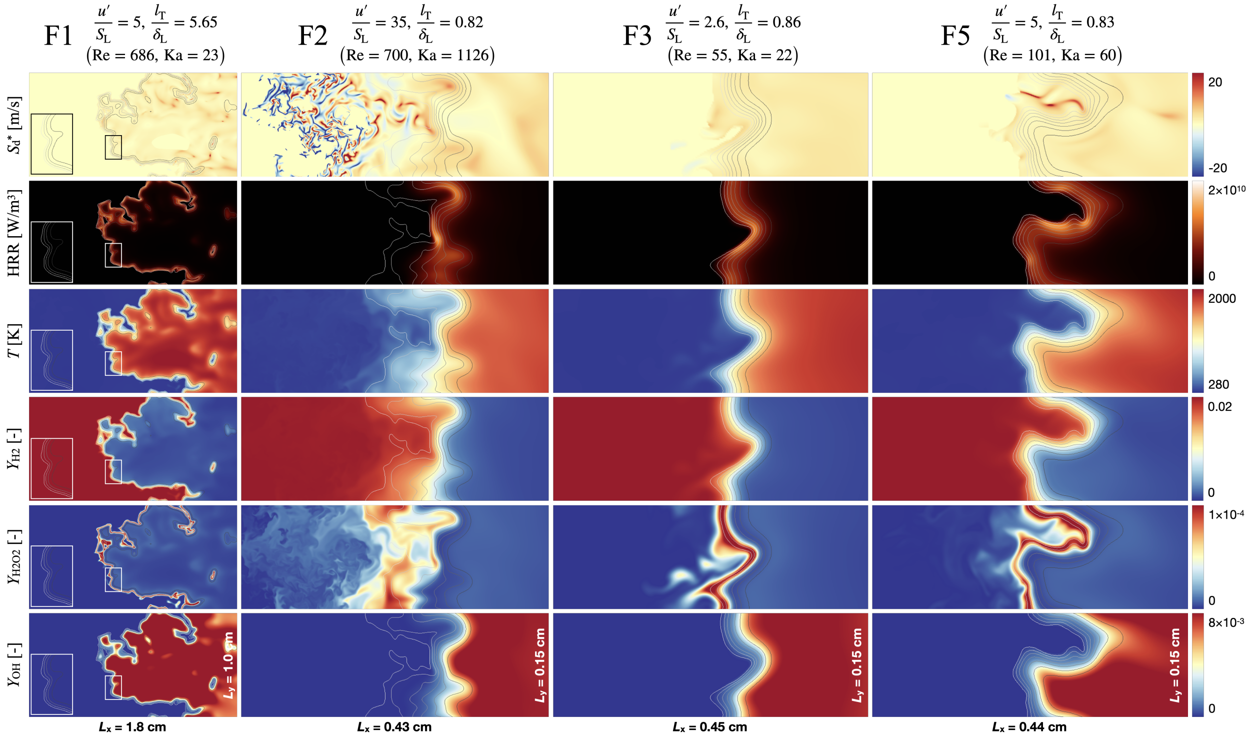

Figure 5: Two-dimensional slices of representative solution variables: the density-weighted displacement speed (S_d^*), heat release rate (HRR), temperature (T), mass fraction of $\mathrm{H_2}$ (Y_H2), mass fraction of $\mathrm{H_2O_2}$ (Y_H2O2), and mass fraction of OH (Y_OH) from top to bottom at $t/\tau_\mathrm{eddy} = 19$ (F1), 53 (F2), 65 (F3), and 182 (F5).

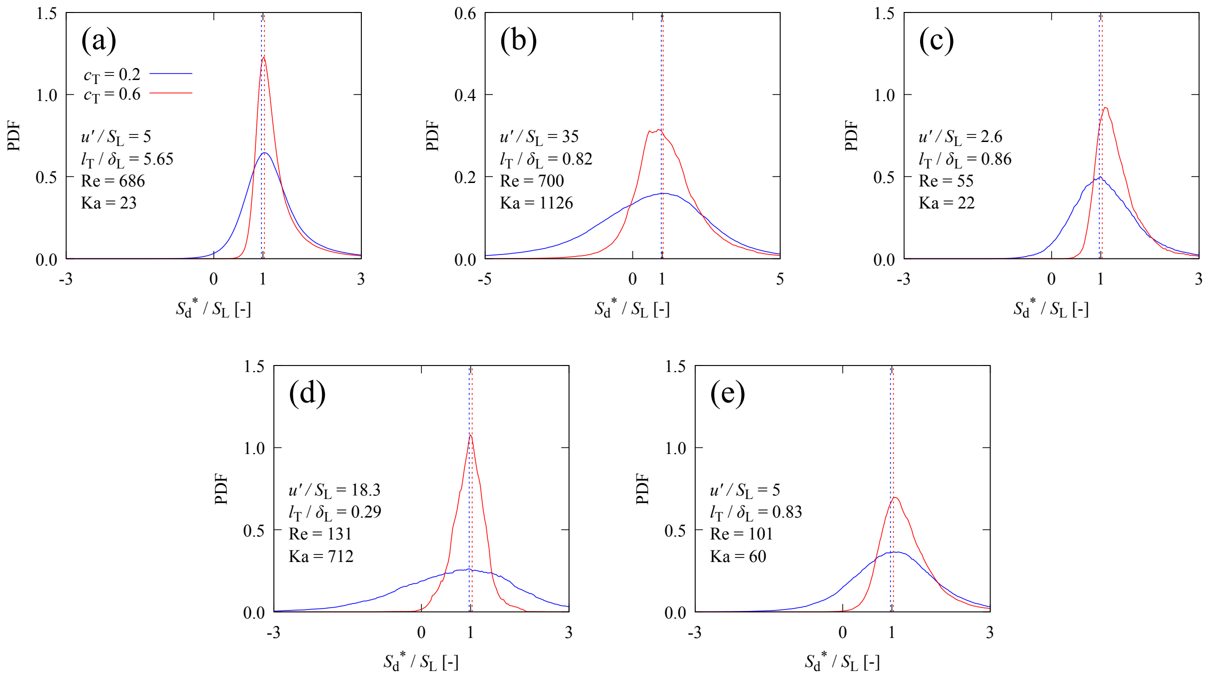

Figure 6: Probability density function (PDF) of the density-weighted displacement speed normalized by the laminar quantity, associated with the progress variable $c_T = 0.2$ (blue) and $c_T = 0.6$ (red) for (a) F1, (b) F2, (c) F3, (d) F4′, and (e) F5. Solid lines are PDF from DNS and dashed lines are the laminar quantities.

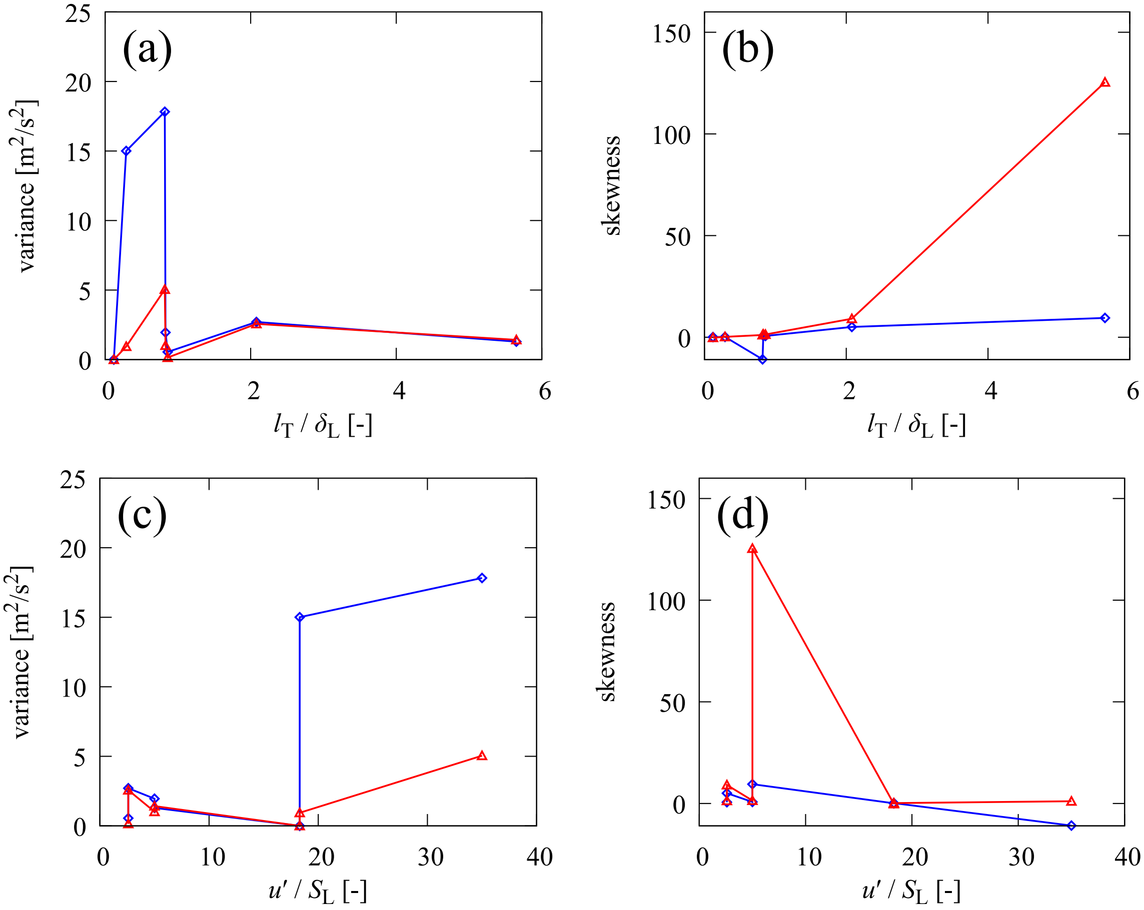

Figure 7: Variance and skewness of S_d^* based on data collected for the time period indicated by the horizontal lines in Fig. 3. (a) and (b) are represented against l_T/δ_L, while (c) and (d) are represented by u'/S_L. Blue lines (diamond symbols) are for $c_T = 0.2$ and red lines (triangle symbols) are for $c_T = 0.6$.

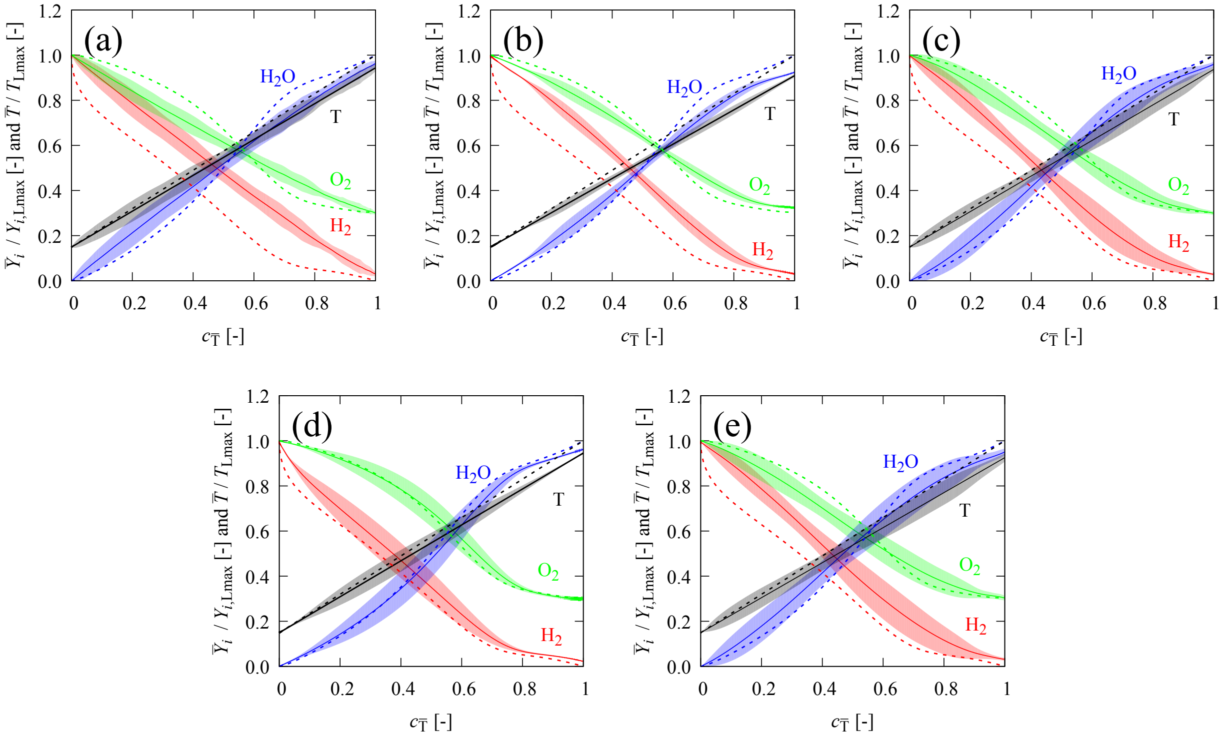

Figure 8: Cross-section average of the temperature and mass fraction of major species for (a) F1, (b) F2, (c) F3, (d) F4′, and (e) F5. Solid lines are mean values for all eddy turnover times, shaded regions are the standard deviation to the mean, and the dashed lines are the laminar quantities.

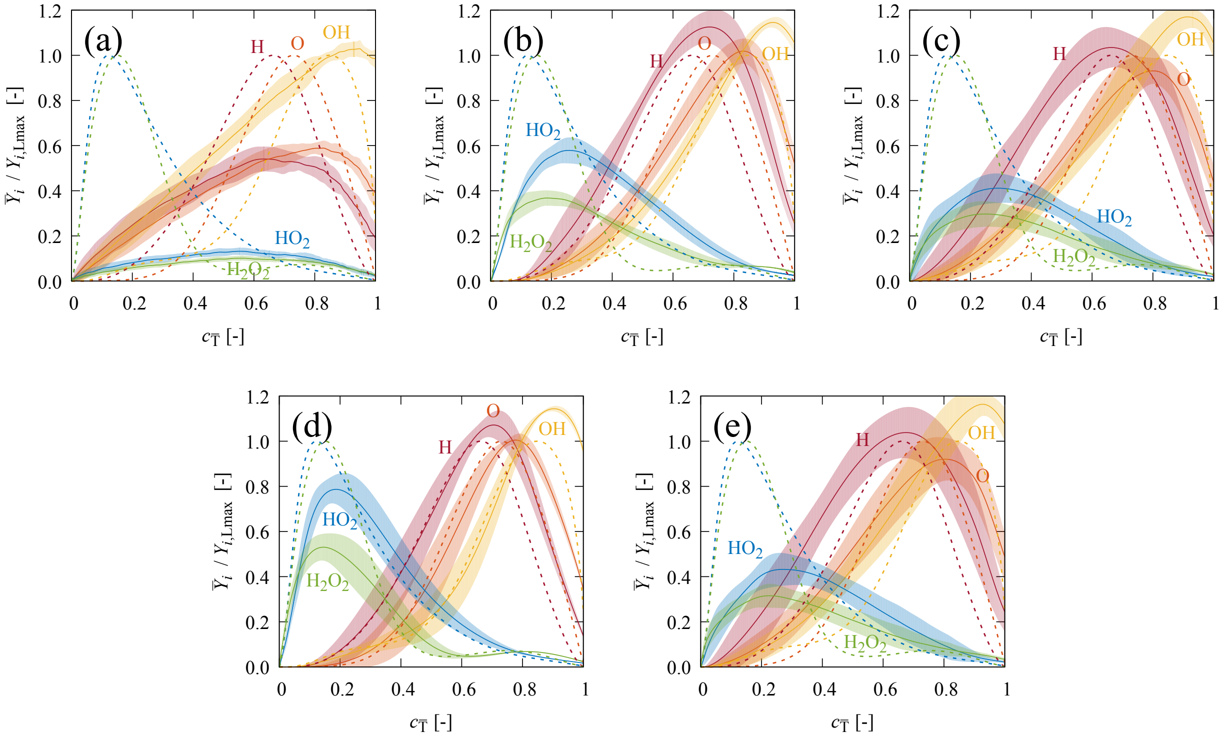

Figure 9: Cross-section average of the mass fractions of intermediate species for (a) F1, (b) F2, (c) F3, (d) F4′, and (e) F5. Solid lines are mean values for all eddy turnover times, shaded regions are the standard deviation to the mean, and the dashed lines are the laminar quantities.

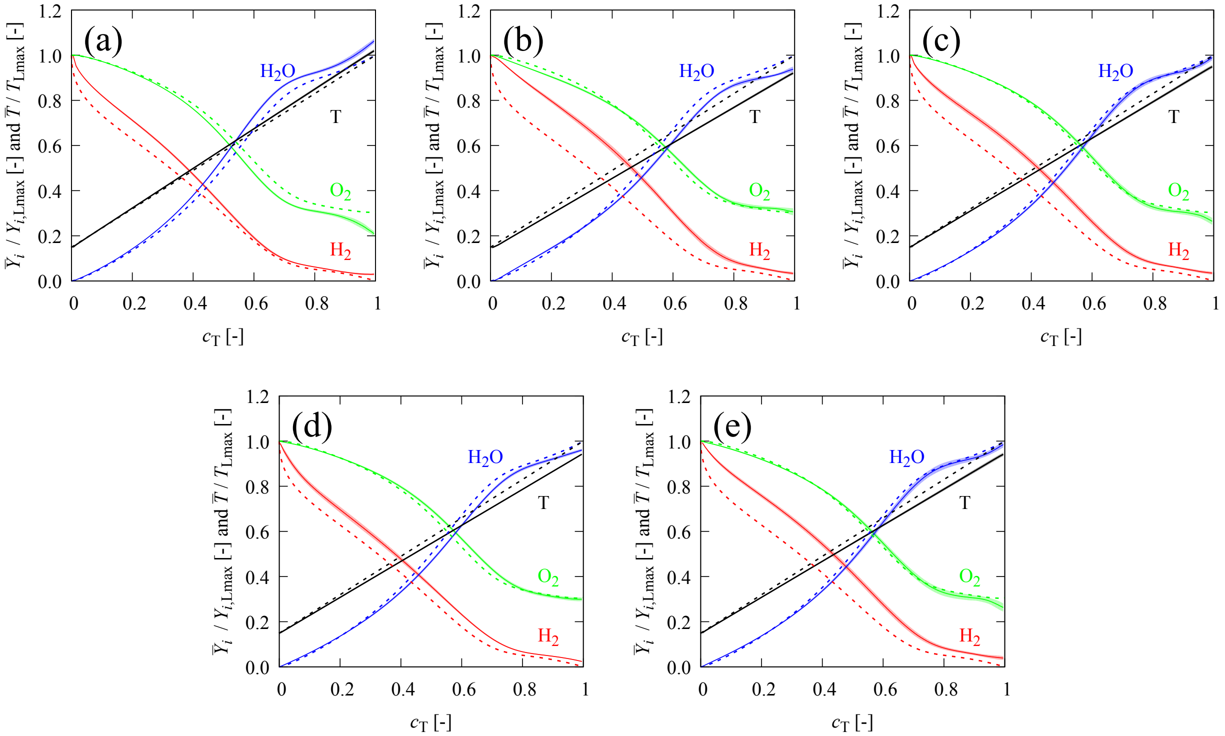

Figure 10: Conditional average of the temperature and mass fraction of major species for (a) F1, (b) F2, (c) F3, (d) F4′, and (e) F5. Solid lines are mean values for all eddy turnover times, shaded regions are the standard deviation to the mean, and the dashed lines are the laminar quantities.

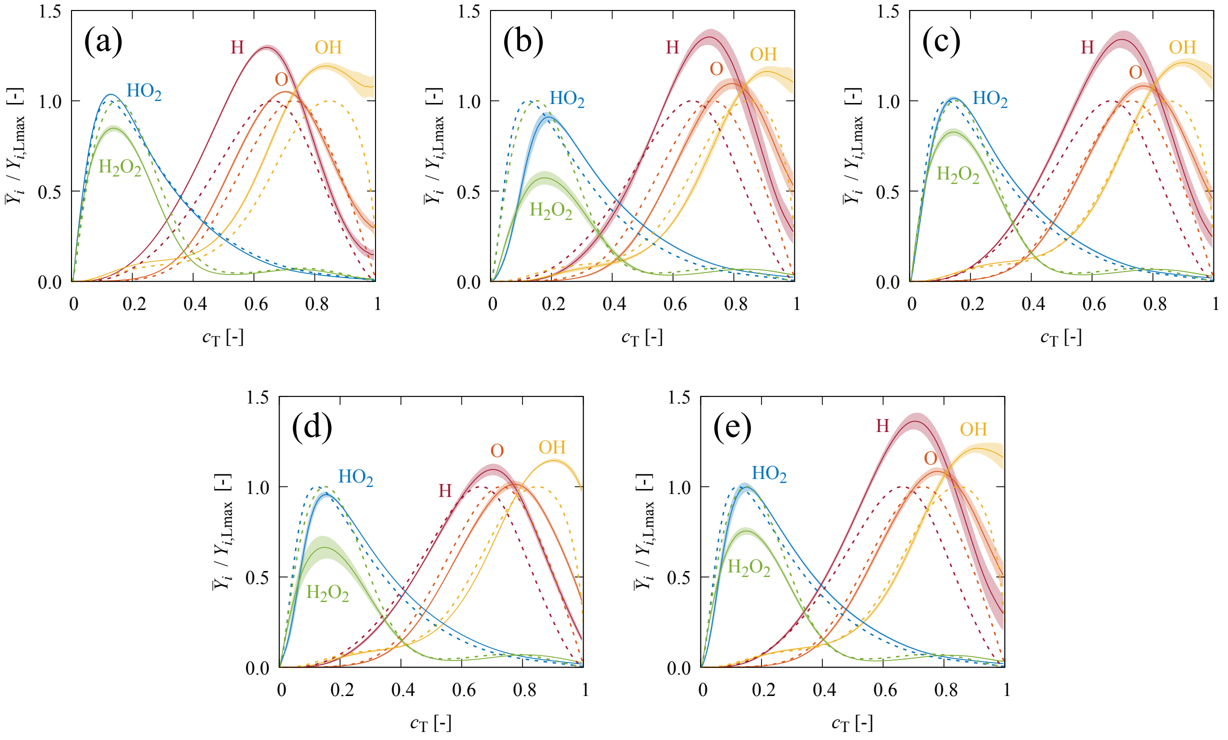

Figure 11: Conditional average of the mass fractions of intermediate species for (a) F1, (b) F2, (c) F3, (d) F4′, and (e) F5. Solid lines are mean values for all eddy turnover times, shaded regions are the standard deviation to the mean, and the dashed lines are the laminar quantities.

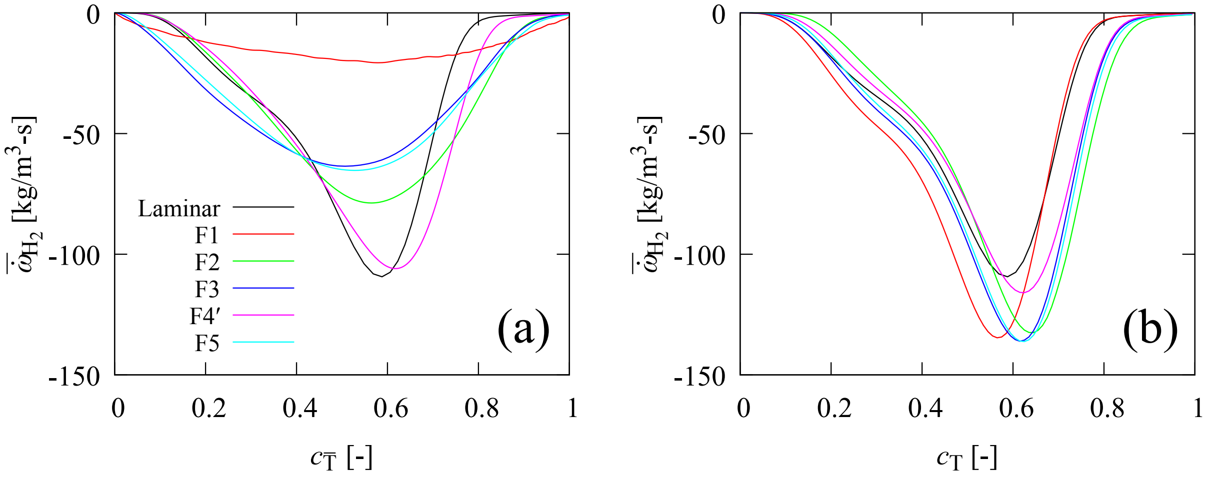

Figure 12: Cross-sectional (a) and conditional (b) average of the consumption rate of the fuel species in comparison with the laminar counterpart.